A&A manuscript no.
(will be inserted by hand later)

Your thesaurus codes are:
08.02.2; 08.14.2.; 02.01.2; 02.19.1; 08.09.2 IP Peg)

ASTRONOMY
AND
ASTROPHYSICS
5.1.1998

A comprehensive study of multi–emission sites in IP Peg ⋆

Sebastian Wolf[1], **Heinz Barwig**[1], **Andreas Bobinger**[1], **Karl–Heinz Mantel**[1], **and Damir Šimić**[2]

[1] Universitäts-Sternwarte, Scheiner Str.1, D–81679 München, Germany
[2] Max–Planck–Institut für extraterrestrische Physik, Giessenbach Str. 1 , D–85740 Garching, Germany

Received 22 October 1997; accepted date

Abstract. We present a comprehensive study of the eclipsing binary IP Peg during quiescence by analysing phase–resolved spectroscopy and simultaneously recorded high–speed–spectrophotometry. By combining both data sets we obtained photometric data of IP Peg with high spectral (1.3Å) resolution. Trailed spectrograms show in unprecedented clearness the well–known Doppler broadened Balmer emission line profiles as well as TiO absorption bands and KI and NaI absorption doublets. By means of Doppler tomography the origin of the *s-wave* in the Hβ, Hα emission lines can be located on the irradiated surface of the secondary star. This indicates an irradiation of the red dwarf during quiescence by an extended accretion disk. Two bright emitting regions superposed to the typical ring–shaped emission of the accretion disk could also be detected. It was possible to analyse separately the eclipse behaviour of the emission lines and of the respective continua. The decomposed continuum light–curves show a second weaker hump phase shifted by 0.5 to the well known orbital hump created by the hot spot. The emission line light curves are dominated by radiation from the accretion disk, showing a slight asymmetry in the V–like eclipse. It is shown, by applying the eclipse mapping method to the emission line light curves, that the bright regions in our high resolution Doppler maps are corresponding to distinct regions in the eclipse maps. In order to compare the two bright emission regions with our spectral data set we reconstructed trailed spectra from the eclipse maps dominated by these multi–emission sites. The following tomographic analysis was in good agreement with our high–resolution Doppler maps. The results obtained from this method are, that IP Peg has a mainly Keplerian accretion disk and that the deviation from the Keplerian field in the hot spot region can be measured by comparing the different Doppler maps with each other. Two theoretical models are discussed to explain the nature and origin of these multi-emission sites, namely a second bright spot model created by a gas stream overflow or by spiral shock waves originating from the interaction of tidal forces of the secondary star with outer regions of an extended accretion disk.

Key words: stars: individual: IP Peg – cataclysmic variables – eclipsing binaries – stars: accretion disks–shock waves

1. Introduction

Cataclysmic variable stars (CVs) are close binary systems, containing a late main–sequence secondary star and a white dwarf primary star. Material is transferred from the Roche-lobe filling secondary star towards the primary star by means of a gas stream. The angular momentum of this stream is too high to fall directly onto the white dwarf. Instead an accretion disk is formed, where the action of viscosity allows the material to slowly spiral inward towards the primary star. A hot spot is formed on the disk at the stream impact region. Most of these binary systems undergo outburst states which vary in duration and brightness. As possible outburst mechanisms two models are under consideration, either a disk instability (e.g. Meyer & Meyer–Hofmeister 1981), which modulates the viscosity of the disk and therefore its ability to transport material inward and angular momentum outward, or an instability of the late–type secondary (Bath & Pringle 1981) which modulates the mass transfer rate of the secondary star to the disk. Dwarf novae are a subgroup of cataclysmic variables showing quasi–periodic outbursts at intervals of tens to hundreds of days in which they brighten by several magnitudes. IP Peg is a well-known deeply eclipsing member of the dwarf nova subclass with an orbital period of 3.79 h (Lipovetskij & Stepanyan 1981, Wolf et al. 1993) and an outburst cycle of about 2.5 months, where the V magnitude (out of eclipse) of this system rises from 14 in quiescence to 12 during outburst (Goranskij et al. 1985). Since its discovery, many approaches were taken to analyse this dwarf nova prototype. Extensive spectroscopic studies of this system were discussed by Marsh (1988), Hessman (1989), Martin et al. (1989), Marsh & Horne (1990), Harlaftis et al. (1994). Photometric observations were made by Szkody & Mateo (1986), Wood &

Send offprint requests to: Sebastian Wolf (*e–mail: wolf@usm.uni-muenchen.de*)

⋆ Based on observations obtained at the German–Spanish Astronomical Center, Calar Alto, Spain.

Crawford (1986), Wood et al. (1989), Wolf et al. (1993), Bobinger et al. (1997). With the advent of sensitive CCD detectors it has become possible to obtain new insights into the accretion mechanisms of this interesting CV. More recent spectroscopic observations (Steeghs et al. 1996; Harlaftis & Steeghs 1997; Steeghs et al. 1997) report the discovery of Balmer emission and slingshot prominences from the secondary star as well as spiral waves in the accretion disk when this system is close to/or in outburst. In this paper we present simultaneously obtained spectroscopic and spectrophotometric data sets of IP Peg in quiescence. With this kind of observations we are able to locate for the first time multi–emission sites in an extended accretion disk during quiescence by applying Doppler tomography and the eclipse mapping method to the data sets. In Sect. 2 we refer on the spectroscopic and spectrophotometric observations of IP Peg and the data reduction procedures used. Section 3 deals with the results and analysis of our data. In Sect. 4 we present Doppler tomograms and eclipse maps of the accretion disk. Finally, in Sects. 5 and 6 a discussion and the summary of this paper are given.

2. Data acquisition and reduction

A special approach to investigate IP Peg was made during an observing campaign in August 1994. We performed simultaneous spectroscopy at the 3.5m and spectrophotometry at the 2.2m telescopes at the German–Spanish Astronomical Center, Calar Alto, Spain.

2.1. Spectroscopy

IP Peg was observed on August 06–09, 1994 with the Cassegrain double beam spectrograph (TWIN) attached to the 3.5m telescope. The blue and the red spectral channels were equipped with low–noise CCDs (TEK#11 and TEK#12) with a pixel size of $24\mu m$ and a CCD size of 1024x1024 pixel. Using a slit–width of $1.''5$ and a spectral resolution of 1.3Å, we chose the spectral range of 4080. . . 5430Å in the blue and 6500. . . 9200Å in the red. The object was trailed along the slit, in order to obtain phase–resolved, high resolution spectra. Exposure times ranged between 600. . . 1800s and the mean trail velocity amounted to 1pixel/22s. Since IP Peg was a secondary target in the V2301 Oph observation campaign (Šimić et al. 1998) we could only cover about 90% of the orbital phase in the blue spectral range. Moreover, due to technical difficulties in observing V2301 Oph the grating angle of TEK#12 was left unchanged (6500. . . 8300Å) in the first observation night, whereas in the following nights the grating angle was adjusted to obtain spectra in the the range between 7200. . . 9200Å. As a result of that, emission as well as absorption lines in the wavelength range of 6500. . . 7200Å were obtained for only 50% of the orbital phase. The trailed spectra were binned in direction of the slit by a factor of 2. Flatfield measurements were taken at the beginning and end of each night, as well as Helium–Argon wavelength calibration spectra which were taken approximately every hour during the night. Further information about the observations is given in Tab. 1. The data reduction included bias–subtraction, flatfield–correction, sky–subtraction, cosmic–ray elimination and wavelength–calibration as described by Horne (1986). After that, the continuum of the spectroscopic data set was calibrated, with our simultaneously obtained spectrophotometric data. By applying this method we were able to correct for intensity variations of the emission lines which might have been caused by poor weather conditions (e.g clouds) or observational difficulties (e.g. variable vignetting of the seeing disk by the slit). Further information is given in Šimić et al. (1998). The trailed spectra were then phase–folded into 100 phase bins using the eclipse-ephemeris of IP Peg from Wolf et al. (1993): HJD 2445615.4224 ($\pm$4) + 0.15820616 ($\pm$4)$\times$ E

Table 1. Journal of spectroscopic observations. B = blue spectral region, R = red spectral region, UT=universal time, IT=integration time

Date	Spectra	Phase range	Start (UT)	IT (s)
06/07.08.1994	B R	0.88–0.93	$00^h04^m22^s$	600
	B R	0.96–0.06	$00^h19^m38^s$	1493
	B R	0.40–0.53	$01^h59^m28^s$	1800
	B R	0.55–0.67	$02^h34^m45^s$	1800
	B R	0.71–0.84	$03^h10^m03^s$	1800
07/08.08.1994	B R	0.63–0.72	$01^h39^m03^s$	1200
	B R	0.73–0.82	$02^h02^m34^s$	1200
	B R	0.83–0.92	$02^h25^m47^s$	1129
	B R	0.93–0.05	$02^h47^m51^s$	1800
	B R	0.08–0.21	$03^h21^m08^s$	1800
	B R	0.22–0.32	$03^h54^m22^s$	1200
08/09.08.1994	B R	0.78–0.86	$01^h01^m35^s$	1013
	B R	0.88–0.96	$01^h21^m54^s$	1026
	B R	0.97–0.09	$01^h42^m33^s$	1665

Table 2. Journal of spectrophotometric observations. UT=universal time, IT=integration time

Date	Start (UT)	Stop (UT)	IT (s)
06/07.08.1994	$23^h55^m40^s$	$04^h22^m01^s$	1
07/08.08.1994	$01^h33^m01^s$	$04^h22^m05^s$	1
08/09.08.1994	$00^h15^m04^s$	$04^h16^m11^s$	1

2.2. Spectrophotometry

Simultaneously with the spectroscopic measurements, we obtained high–speed (time resolution : 1s) spectrophotometric data with MEKASPEK attached to the 2.2m telescope at the Calar Alto Observatory. This 4 channel fiber–optic spectrophotometer was developed at the Universitäts–Sternwarte München and has the following properties : Simultaneous measurements of object, two comparison stars and sky background within the

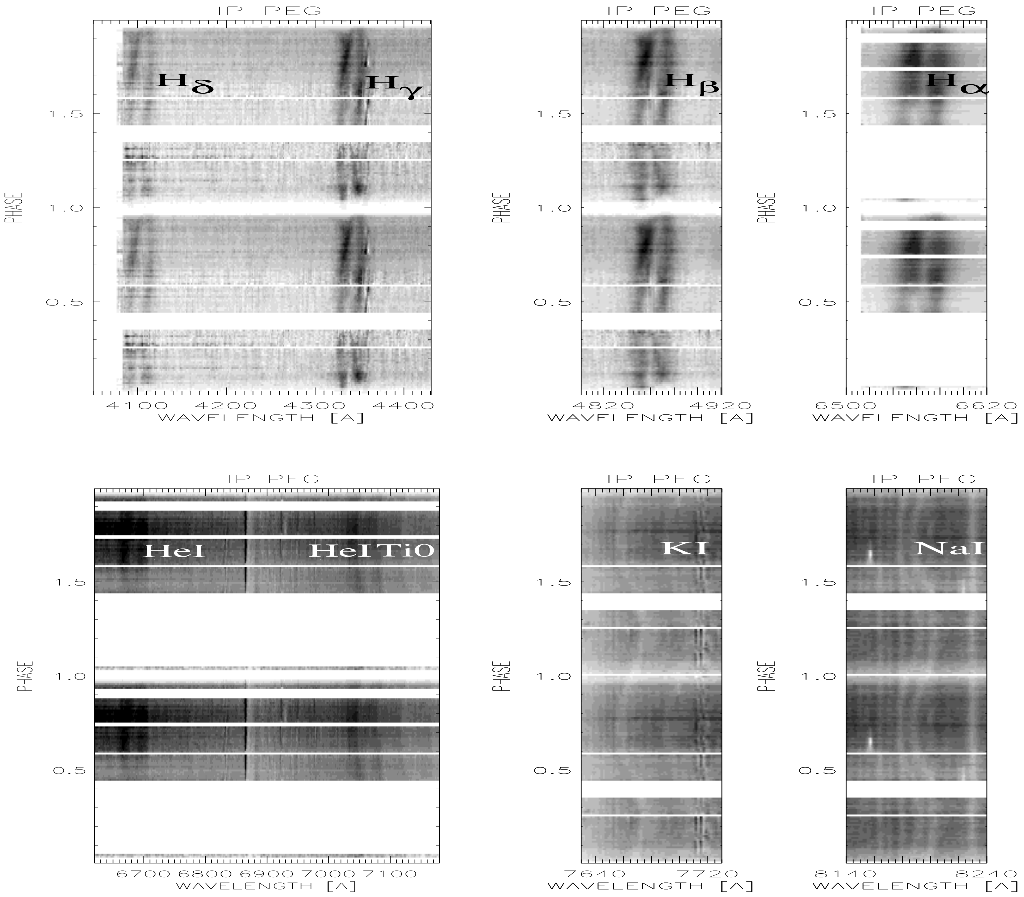

Fig. 1. Trailed, photometrically calibrated, high–resolution spectra of IP Peg derived by phase–averaging the spectra into 100 phase bins. The dynamic range of each grey–scale plot was chosen appropriately to emphasize the individual features of the emission and absorption lines, where the phase runs along the ordinate and the wavelength along the abscissa. Note, that the *s-wave* in the Balmer lines reflects the orbital motion of the secondary star as represented in the KI and NaI absorption lines. The faint, straight emission lines around 4360Å and 6880Å represent weak remnants of atmospheric emission lines, whereas the straight absorption line at around 8200Å is due to an atmospheric oxygen absorption band.

spectral range of 3700. . . 9000Å at a spectral resolution of λ / $\Delta\lambda \approx$ 50. The photon–counting two–dimensional detector (MEPSICRON) has a time resolution of up to 5ms with no deadtime during readout. Furthermore, MEKASPEK performs a correct treatment of atmospheric extinction effects and allows an accurate colour transformation to any broadband photometric system. A specially developed online–graphics–system allows to examine in realtime the observed spectra and light curves of object, comparison stars and sky background in selected spectral regions. For more details see Mantel et al. (1993b) and Mantel & Barwig (1993). Atmospheric effects are eliminated using the so–called $standard\ reduction$ (Barwig et al. 1987) which subtracts the sky background of each colour channel from object and comparison star and divides the object by the comparison star measurements afterwards, therefore enabling photometric measurements even under non–photometric conditions. Due to the properties of MEKASPEK, it is also possible to investigate separately the Balmer emission lines and the respective continua. However, because of the short integration time (1s) the single spectra were quite weak. In order to improve the S/N, the spectra were binned in time by a factor of 20 for a first presentation in Sect. 3.5. Instead of dividing by the comparison star, we confined the reduction to sky–subtraction only. Non–photometric parts of light curves were excluded. The emission lines were extracted from the spectrophotometric data set by subtracting an interpolated continuum. For a detailed analysis of these light curves in Sect. 4.2. a bin factor of 6 in time was used and the $standard\ reduction$ was applied again to the data set. More information is given in Sect. 4.2. The details of the simultaneous spectrophotometric observations are listed in Tab. 2.

3. Analysis and results

3.1. The trailed spectra

A detailed survey of individual emission lines, that is to say, the stronger lines Hδ, Hγ, Hβ, Hα, HeI ($\lambda\lambda$ 6678, 7065), and

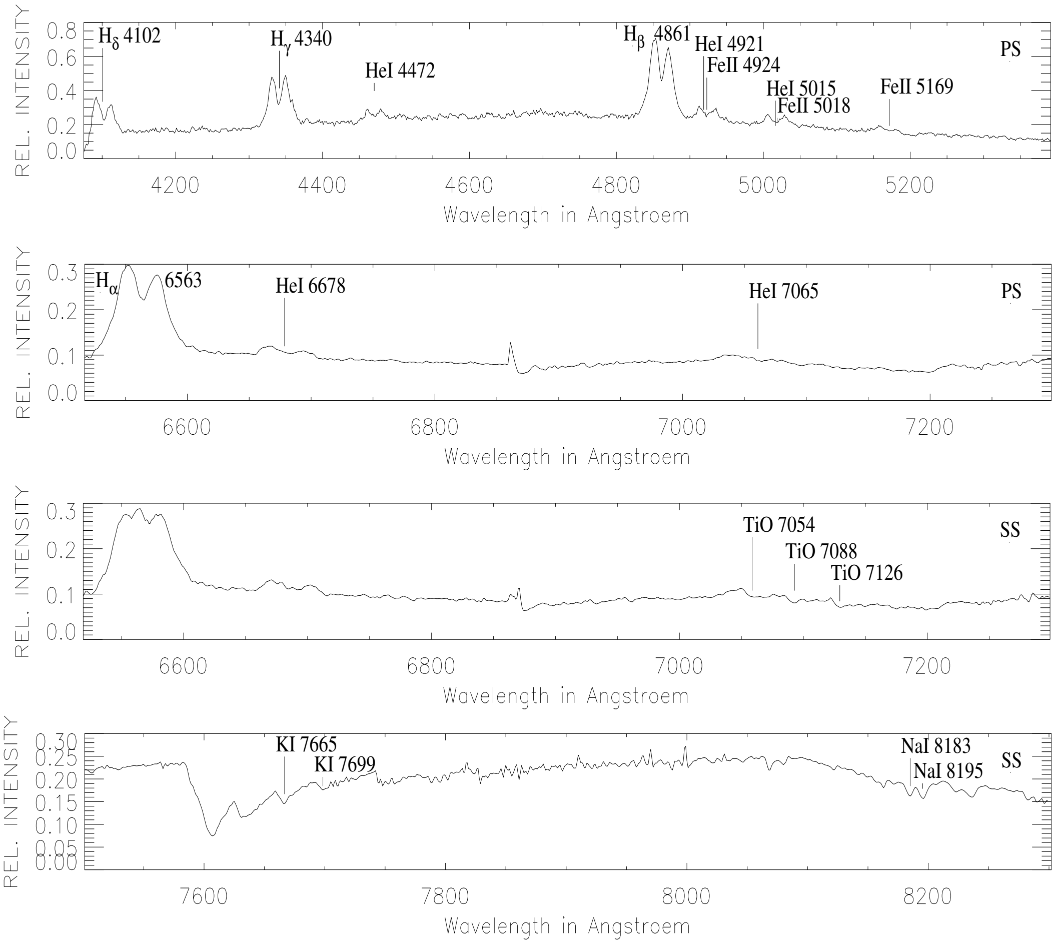

Fig. 2. Mean orbital spectra of IP Peg in the blue spectral range (first upper panel) and the red spectral range (lower three panels) after radial–velocity–correction, in order to emphasize either the PS (primary star: additional shift of 168 $\mathrm{kms}^{-1} \cdot \sin\phi$) or the SS (secondary star: additional shift of –280 $\mathrm{kms}^{-1} \cdot \sin\phi$). Outstandingly visible in the SS-corrected spectra is a spike in Hα between the double–peaked emission line components which represents emission from the irradiated face of the secondary. The spikes around 6870Å and between 7700Å. . . 8050Å are faint reduction remnants of atmospheric emission lines, whereas the absorption dips around 7600Å and 8200Å represent atmospheric oxygen absorption bands.

the absorption bands of TiO ($\lambda\lambda$ 7054, 7088 and 7194), as well as the absorption doublets of KI($\lambda\lambda$ 7665, 7699) and NaI ($\lambda\lambda$ 8183, 8195) is shown in Fig. 1, all with a phase resolution of 100 phase bins. The dynamical grey–scale range was set intentionally, in order to emphasize the individual line features. The emission lines of HeI(λ 4472), HeI (($\lambda\lambda$ 4921, 5015) blended with FeII ($\lambda\lambda$ 4924, 5018)) and FeII (λ 5169), were excluded from further investigations due to the poor S/N. The trailed spectra reveal the typical Doppler–separated emission line components characteristic of a CV with a high inclination. Also clearly visible is the rotational disturbance, in which the blue–shifted emission line component is eclipsed before the red–shifted emission line component, a clear indicator for prograde disk rotation (Marsh 1988). The sinusoidal velocity shifts of the emission line peaks mirror the orbital motion of the white dwarf. Another interesting feature is the so-called *s-wave*, which normally has its origin in the impact site, where the gas stream hits the disk. This feature moves back and forth between the two Doppler components in an S–like manner. In our case, we are able to assign the *s-wave* to the secondary star, because after comparing the feature with the progression of the NaI and KI doublets we found it to be in agreement with the orbital motion of the secondary star. The illumination of the secondary star which manifests itself in the mentioned *s-wave* of the Balmer lines might be invoked by either the hot spot on the rim of an extended accretion disk or by the boundary layer. Further proof for these assumptions are given by observations of IP Peg in outburst obtained by Nogami (1995) almost three weeks after our observation run. The long outburst reached its maximum luminosity on August 28, whereas the analysis of the eclipse light curves revealed an expansion of the accretion disk during the pre–maximum phase. More details are given

in Nogami (1995). The co–existence of strong emission and absorption lines is not unusual for IP Peg. Martin et al. (1989) were able to detect absorption lines (NaI($\lambda\lambda$ 8183, 8195)) and a HeI (λ 7065) emission line with a particular strong *s-wave* originating from the red star when this system was on the decline from an outburst and still one visual magnitude above the minimum (out of eclipse) brightness. Such a signature might also be an indicator for this binary being prior to an outburst.
The radial velocity semi–amplitudes of the strong absorption line doublets (NaI and KI) reflect the orbital motion of the secondary star. The second KI absorption line appears somewhat weaker, which is due to irradiation from the disk. This illumination effect ionizes KI on the inner face of the secondary and therefore decreases the strength of the doublet. For a detailed examination of this effect see Martin et al. (1989).
Also visible are the weak TiO–bands, characteristic of M dwarf stars which considerably blur the adjacent HeI (λ 7065) emission line. The radial velocity semi–amplitude of this emission line resembles those of the KI and NaI absorption doublets, though its amplitude seems to be lower. We note, that this behaviour is almost certainly caused by the above mentioned blurring effect.

3.2. The mean orbital spectra

In Fig. 2 we present radial velocity–corrected, mean orbital spectra in the blue (4080. . . 5350Å) and in the red spectral range (6500. . . 8300Å) in order to distinguish spectroscopic evidence either of the primary star (PS) or the secondary star (SS). To accentuate the PS or the SS the spectra were shifted with a radial velocity of 168 $\mathrm{kms}^{-1} \cdot \sin\phi$ and –280 $\mathrm{kms}^{-1} \cdot \sin\phi$, respectively (for information about the determination of the radial velocities see Appendix A.).
The mean optical spectra of IP Peg in quiescence are characterized by a flat continuum and strong double peaked emission lines in the blue spectral range of 4050Å. . . 5400Å. In the red spectral range between 6500Å. . . 8300Å the dominance of the secondary star becomes evident. Double peaked emission lines could be detected up to 7100Å but further on the continuum becomes obscured by TiO–bands and strong KI And NaI absorption doublets. We identified lines of the Balmer series (Hδ, Hγ, Hβ and Hα) as well as of HeI ($\lambda\lambda$ 4921, 5016) blended with FeI ($\lambda\lambda$ 4924, 5018) and the single lines of HeI ($\lambda\lambda$ 4472) and FeII (λ 4686). Following absorption bands could be detected TiO ($\lambda\lambda$ 7054, 7088, 7126) as well as the absorption line doublets KI ($\lambda\lambda$ 7664,7699) and NaI ($\lambda\lambda$ 8183, 8195) typical for a late type M dwarf star.
The SS–corrected spectra show a peaked narrow emission between the double peaked emission components of Hα confirming our assumption that the *s-wave* present in the Hβ and Hα emission lines has its origin on the secondary star.

3.3. The light curves

Spectrophotometric observations of IP Peg were obtained with MEKASPEK over three consecutive nights (06–09 Aug., 1994). Almost four eclipses could be acquired, though only the last night turned out to be photometric. The data set was reduced as described in Sect.2.2 using the $standard\ reduction$. The reduced light curves of each night in integral light are presented in Fig. 3.
The light curves of IP Peg presented in this paper are typical of a dwarf nova in quiescence. They show the characteristic strong orbital hump from the hot spot which originates on the outer rim of the accretion disk due to interaction with the gas stream. The hump disappears quite suddenly and unfortunately coincides with the ingress of the white dwarf.
The white dwarf egress step on the other hand is clearly resolved, followed by the egress of the hot spot and the remaining part of the accretion disk.

3.4. The decomposition of light curves

As explained in Sect.2.2., using MEKASPEK we were able to extract Balmer lines from the continuum. Emission lines of IP Peg are thought to be arising mainly in the accretion disk and partly in cooler regions of the hot spot, whereas the white dwarf and most of the hot spot dominate in the continuum.
For the decomposed light curves a lower time resolution (20s) was chosen, in favor of a better S/N. Still, the signal in the emission line light curves is quite noisy and useful information can only be obtained by phase–folding all acquired light curves at the orbital period with the already mentioned (Sect. 2.2) ephemeris of Wolf et al. (1993). In order to further increase the S/N, the individual phase diagrams of the Balmer lines and the underlying continuum were summed up as shown in Fig. 4.
The continuum light curves clearly show features of the primary star and the hot spot as explained in the above section. A second weaker hump around phase 0.4 could be detected which was only partially seen in the integral light curves in Fig. 3, since the observation runs were suspended in this phase–range for calibration measurements.
The second hump can be interpreted as changing viewing aspect of the hot spot which, due to the inclination of i $\approx 80^o$ shines through/above the optically thin accretion disk.
The light curves of the Balmer lines differ significantly from those of the continua. Their progression clearly indicates the origin in the accretion disk mostly. The eclipse has a V–like structure which points out to a nearly symmetric disk with a flat, radial temperature distribution.
We note, that there is a slight asymmetry in the emission line light curves, reflecting an non–uniform flux distribution in the disk, an effect also noted by Marsh (1988).
The origin of this asymmetry will be analysed and discussed in Sects. 4 and 5.

4. The detection of multi–emission sites in a quiescent accretion disk

4.1. Doppler tomography

Doppler tomography is an useful tool to extract further information on CVs from trailed spectra. This indirect imaging

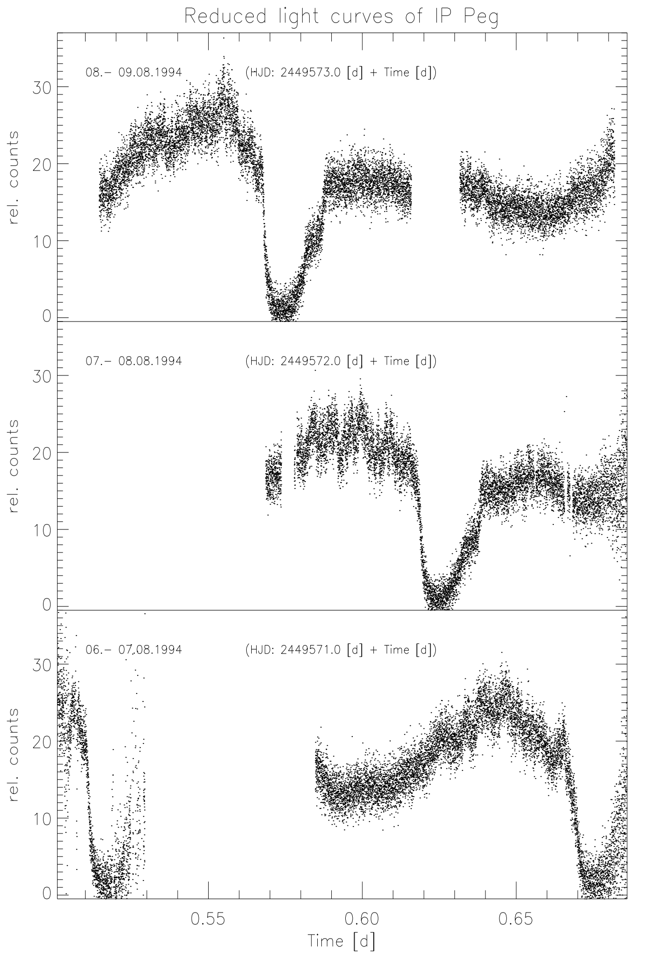

Fig. 3. Reduced light curves of IP Peg in integral light taken on the indicated dates. The time scale has been adjusted to the longest run in order to compare the light curve features from the individual nights. Gaps within the light curves are due to calibration measurements. The same scaling of the Y–Axis has been taken for all plots, because we wanted to check night to night flux variations. Every data point represents an integration of 1s.

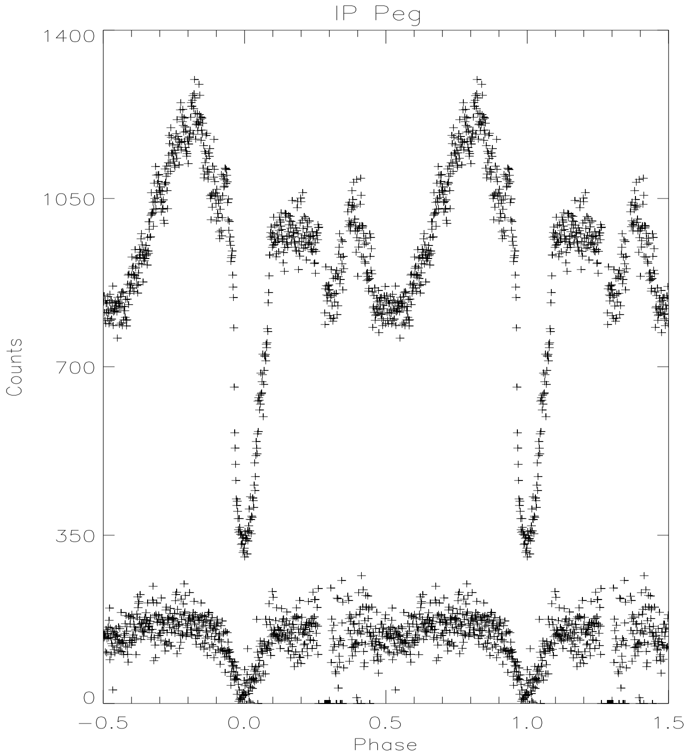

Fig. 4. Summed phase diagrams of the emission lines Hγ, Hβ, Hα (lower light curve) and of the underlying continua (upper light curve, plotted with an offset of 300 counts). Integration time and bin size are 20s. The phase–range is repeated for clarity and count rates are set to the same value in order to emphasize the presence or absence of features of the different contributing light sources (accretion disk or white dwarf/hot spot). The gap around phase 0.3 is due to a lack of measurements.

technique which was developed by Marsh & Horne (1988) uses the velocity profiles of emission–lines at each phase to create a two–dimensional intensity image in velocity–space coordinates (V_X, V_Y). Therefore, the Doppler tomogram can be interpreted as a projection of emitting regions in cataclysmic variables onto the plane perpendicular to the observer's view. The Doppler map is a function of the velocity (V_X, V_Y), where the X–axis points from the white dwarf to the secondary star and the Y–axis points in the direction of the secondary's motion. An image pixel with given velocity coordinates (V_X, V_Y) produces an S–wave with a radial velocity

$$V = \gamma - V_X \cos(2\pi\phi) + V_Y \sin(2\pi\phi) \qquad (1)$$

where γ denotes the system velocity and ϕ the phase. Simply speaking, a Doppler map displays line profile information from all binary phases in a single image, thus providing a collective view created by the entire data set. To accomplish this, a linear tomography algorithm, the Fourier–filtered back–projection (FFBP) is used, which is described in detail e.g. by Horne (1991). The double peaked line profiles of an accretion disk become a diffuse ring–like region in a Doppler map (or tomogram) which is mostly displayed as a grey–scale image. Assuming a Keplerian velocity field, emission originating near the center of the system has a larger velocity and thus appears in the outer regions of the map. Therefore, an image in such a representation is turned inside–out. A helpful assistance in interpreting Doppler maps are additional inserted plots which mark the position of the secondary star and the ballistic trajectory of the gas stream. As an additional help we have plotted the accretion geometry of IP Peg in velocity as well as in spatial coordinates in Fig. 5.

For the tomogram analysis we restrict ourselves to the three Balmer lines Hγ, Hβ, Hα. No reasonable Doppler maps could be produced either for Hδ, because this emission line was too close to the edge of the CCD, or for the blended HeI ($\lambda\lambda$ 4921, 5016) emission lines which had a too poor S/N. Since we cannot assume any relation between position and

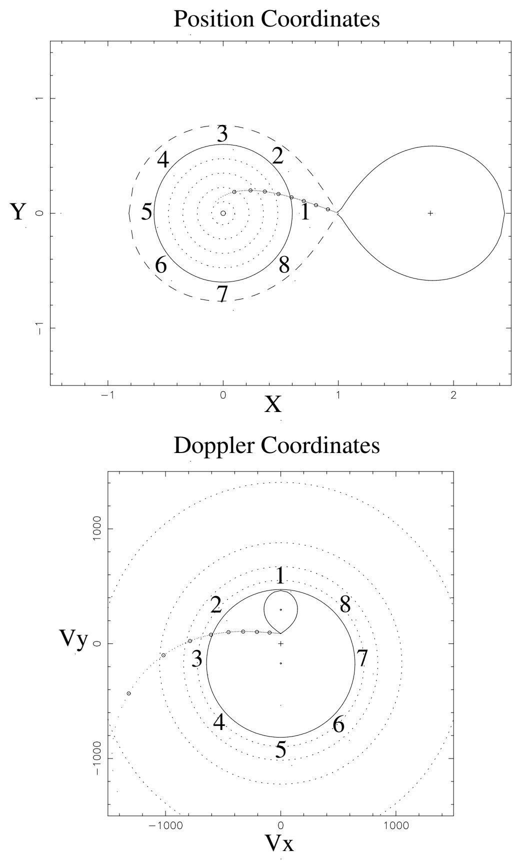

Fig. 5. Display of the relationship between spatial coordinates (top panel) , which later also applies for the eclipse maps, and velocity coordinates in a Doppler map (lower panel). The loci of the primary and the secondary star are denoted by a cross and an empty circle in the top panel, whereas they are marked by two dots in the lower panel, respectively. Their Roche lobes are displayed as solid line (secondary) and dashed line (primary) whereas the outer radius of the accretion disk is plotted as solid line. The mass center and the inner Lagrangian L_1 point are displayed by a dot in the upper image and by a cross in the lower image, respectively. The ballistic trajectory of the gas stream moves in an arc–like manner from L_1 towards the primary star. Disk rings at different radii(top) map into ring at the corresponding Keplarian velocity, resulting in an inside–out picture of the disk since the inner disk has a higher velocity. Arranged in an anti–clockwise manner around the binary sketch are eight selected phase points in velocity as well as in spatial coordinates.

velocity during eclipse we constrained our data set by removing eclipse spectra between the phase–ranges $\phi = 0.95 \ldots 0.05$. Before computing the tomograms we subtracted the underlying continuum from the individual emission–lines, since their line–flux is the quantity needed to produce these maps. This was done by subtracting from each pixel row of the trailed spectra the according median of the intensity. The emission lines in V, ϕ–coordinates are displayed in Fig. 6 and the corresponding Doppler maps in velocity coordinates (V_X, V_Y) are shown in Fig. 7 as grey–scale–plots. It should be noted, that we achieved a FWHM resolution of 200 kms^{-1} in the central regions of the tomograms, whereas at higher velocities ($\approx$ 800 kms^{-1}) the resolution of the maps suffered a considerable degradation.

Furthermore, the emission lines might be blurred by the so–called 'gamma–smearing' effect which is explained in detail by Diaz & Steiner (1994). Gas moving with a velocity V_Z perpendicular to the orbital plane generates a shift $\gamma = V_Z \cos i$ which blurs the corresponding feature in the Doppler image in a ring–like manner. The linear structures in the high velocity region of the map are sampling artifacts (aliasing streaks) which are not taken into account in the further interpretation. For a detailed discussion about sampling artifacts see e.g. Robinson et al. (1993).

The schematic overlay of the Roche–lobe and the gas stream trajectory is a function of K_1 and K_2 which were derived in Appendix A. The center of mass and the location of the white dwarf are marked respectively by a cross and a point located below the Roche lobe, whereas the ballistic stream is represented by an arc originating from the secondary's lobe at the inner Lagrangian point. This arc is calibrated every $0.1 R_{L_1}$ (open circles) as it is accelerated towards the primary star. Additionally, the velocity of the disk along the path of the gas stream is also plotted in each Doppler map.

The Doppler tomograms of our data show at first sight the typical ring–like distribution expected from the double peaked Balmer emission lines. Superposed to this diffuse ring are two bright emitting regions and a weak spot. The larger one has velocity coordinates of $V_X \approx 200 \ldots 800$ kms^{-1}, $V_Y \approx -900 \ldots 300$ kms^{-1}. The smaller one has the velocity coordinates of $V_X \approx -200 \ldots -800$ kms^{-1}, $V_Y \approx 200 \ldots 600$ kms^{-1} .

Due to the asymmetric brightness distribution in the trailed spectra around phases 0.8 (stronger emission line–flux) and 0.3 (weaker emission line–flux) in Fig.6 we conclude that the mentioned bright emitting regions in the Doppler maps have an anisotropic radiation pattern.

The weak emission spot with velocity coordinates of $V_X \approx 0$ kms^{-1}, $V_Y \approx 300$ kms^{-1} can be explained with emission coming from the irradiated face of the secondary and corresponds to the *s-wave* crossing the Doppler peaks between phase ranges $\varphi \approx 0.4 \ldots 0.6$ in Fig. 6. Irradiation of the secondary star by the boundary layer was offered as plausible mechanism in Marsh & Horne (1990). Simulations of Doppler maps of IP Peg close to an outburst, performed by Harlaftis et al. (1994) showed that emission features of the secondary can be hidden in trailed spectra. Due to effects of noise and strong emission of the disk this feature can be better resolved in the Doppler maps. We can contribute our feature also to secondary emission probably caused by irradiation of an extended accretion disk.

The large emission spot was also observed in quiescent data by Marsh & Horne (1990) and Harlaftis et al. (1994). This feature was explained by Harlaftis et al. (1994) as the red component of the line profile being slightly stronger than the blue component. Recent high resolution Doppler maps of IP Peg in outburst show two large bright emission regions diametrically opposed to each other (Steeghs et al. 1997; Harlaftis & Steeghs 1997) looking quite similar to our observed large spot. These features are interpreted as two spiral arms in the outer disk whose excitation is due to tidal forces of the secondary star. This detection was possible, because the accretion disk radius was quite large.

We interpret our large bright spot with the probable beginning of the formation of such a spiral arm. We note, that according to Smooth Particle Hydrodynamics (SPH) simulations performed by Armitage & Livio (1996) a second bright spot might also be created by the impact of returning material from a mass overflow of the gas stream. A clear allocation of both emitting bright regions is given in the next section where eclipse maps in position coordinates are presented.

The smaller bright emission region can be unequivocally contributed to emission from the hot spot on the outer regions of the accretion disk.

The tomogram of Hγ (Fig. 7) shows the typical ring–like distribution of the Doppler broadened emission line profile as explained above. An interesting exception is that we could not find evidence for secondary emission in this tomogram. Both bright emitting regions are clearly represented, though not so intense as in Hβ. The trajectory which marks the velocity of the disk along the path of the gas stream fits the small spot well and reflects the penetration of the stream into the disk.

Comparing the Hβ with the Hγ (Fig. 7) Doppler map, we find some differences. The emission from the secondary is clearly evident and the emitting regions are more intense in Hβ.

The Hα tomogram seems to be more blurred which may be due to the above mentioned 'gamma–smearing' effect. Although we could obtain only 50% phase coverage of the Hα (explanation given in Sect.2.1.) the back–projected Doppler map resembles the other maps very well and we can still distinguish the same features (extended bright areas) as well as strong emission from the secondary just like in the Hβ map.

4.2. Eclipse mapping

Up to now two different methods have been developed to investigate CVs, namely Doppler Tomography and eclipse mapping (Horne 1985, Horne 1995, Horne & Cook 1985, Horne & Marsh 1986, Baptista & Steiner 1993, Horne & Stiening 1985, Kaitchuck et al. 1994, Rutten et al. 1992a, Rutten et al. 1992b). The first one was discussed in the previous sections, this section is dedicated mainly to the last one.

4.2.1. Method and data

In order to investigate IP Peg with the eclipse mapping tool, we used a slightly modified version of the eclipse mapping algorithm developed by Keith Horne (Horne 1985).

The eclipse mapping method employs the maximum entropy fitting package MEMSYS (Skilling & Bryan 1984) to interprete observed eclipse light curves in terms of intensity and brightness temperature maps of accretion disks. A two dimensional grid, located in the orbital plane and centered on the white dwarf undergoes an eclipse by the secondary star to produce an artificial light curve, whereby all pixels are assumed to have the same brightness at all phases. The intensities of the pixels are adjusted until the artificial light curve fits the observed one within a maximum allowed χ^2 deviation. Since such a χ^2-fit does not produce an unique solution, an image-entropy is defined on the grid of pixels and maximized with respect to a default image. As a result a map is obtained which is as close as possible to the default map and which fits the data within the allowed χ^2-deviation.

The eclipse mapping method used by us is different with respect to the adopted geometry for the reconstructions. Instead of a flat grid, a three dimensional disk with a constant disk opening angle and an outward facing "ribbon" at a certain disk radius was used. We used a polar grid for our disk, and a ribbon which is build up by three pixel rows in order to match the outer disk to the rim-ribbon as smooth as possible. As an opening angle we chose 1° up and down, in order do hold the disk as geometrically thin as possible and to provide pixels for the anisotropic light mapping.

Our improved method addresses two specific problems with the original eclipse mapping method. First, light curve variations in IP Peg which are due to anisotropic light sources, like the already explained hump (Sect.3.4), cannot be mapped due to the assumed isotropic radiation of the pixels. This problem is usually solved by decomposing the light curve into its different parts, like the white dwarf light curve, the hot spot light curve and the disk light curve (Wood et al. 1992). But this requires a very high signal to noise ratio and a clear separation of all ingress and egress features of every component in the light curve. This is unfortunately not the case for IP Peg.

First, hot spot and white dwarf ingress take place almost simultaneously and are therefore not distinguishable and our signal to noise ratio of our data is also low.

Second, there is only one-dimensional information available from the observed light curve for the reconstruction of the two-dimensional disk. Therefore, additional constraints have to be introduced. This is done by manipulating the default image in a special manner, leading to the conclusion that the final result depends on the default image and the way it is created.

Usually, the so–called most nearly axisymetric default method is used, which means the maximization of the entropy with respect to azimuth. This method is the best one to reconstruct the global radial structure of the disk, but all narrow structures are smeared out in a ring–like way.

Another method, the so called smoothest default method, holds the true position of the narrow structures, but it disturbs the radial profile by smearing out the structure along the ingress-egress-shadow arcs thrown by the secondary over the disk.

We used the smoothest method, because we are more interested in the true locations of structures in the disk. These details are discussed thoroughly in Bobinger et al. (1997).

As explained in Sect. 2.2., MEKASPEK produces high speed photometric data which allows to follow fast variations in CVs and holds a high enough spectral resolution to follow the Balmer emission lines from Hα up to Hγ during all phases of the binary's period.

To get light curves for the eclipse mapping tool we binned our dataset by a factor of 6 in order to have a high-enough time resolution and applied again the *standard reduction* (see

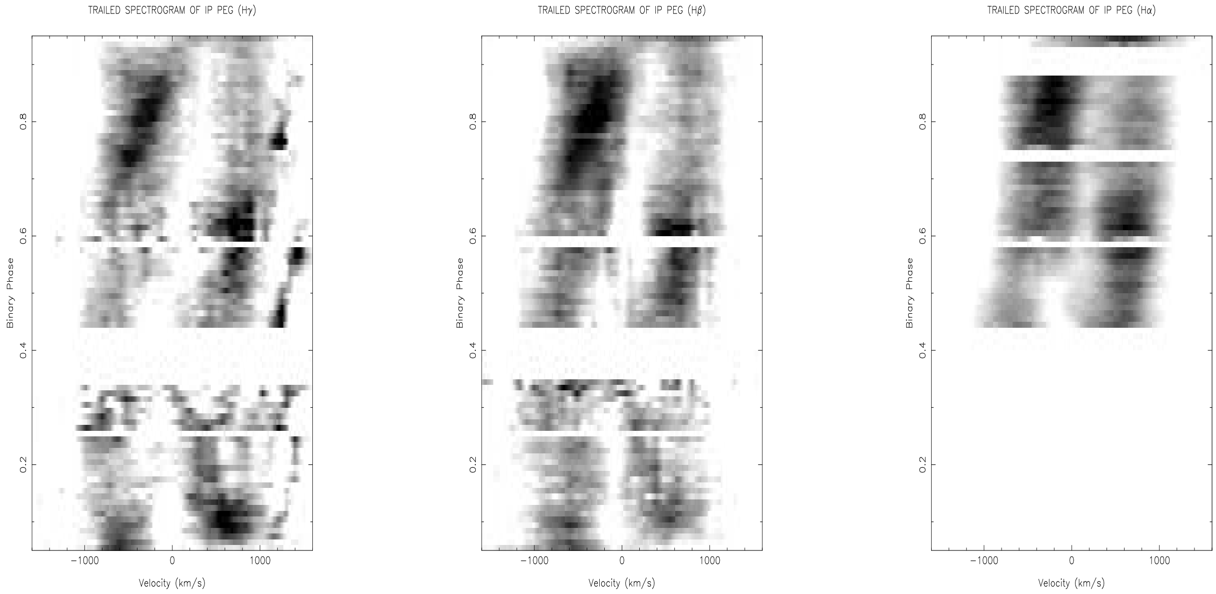

Fig. 6. Zoomed gray–scale representations of continuum–subtracted, photometrically calibrated, high–resolution spectra of the prominent Balmer lines Hγ, Hβ and Hα. The emission lines are plotted in $v,\ \phi$–coordinates. Not covered phase–ranges are marked with white empty rows. The eclipse spectra have been removed, since we assume no relation between position and velocity. The fragmented line appearing in the Hγ spectra is a remnant of a night sky line. Note that we could obtain only 50% phase coverage of Hα (an explanation is given in Sect.2.1.).

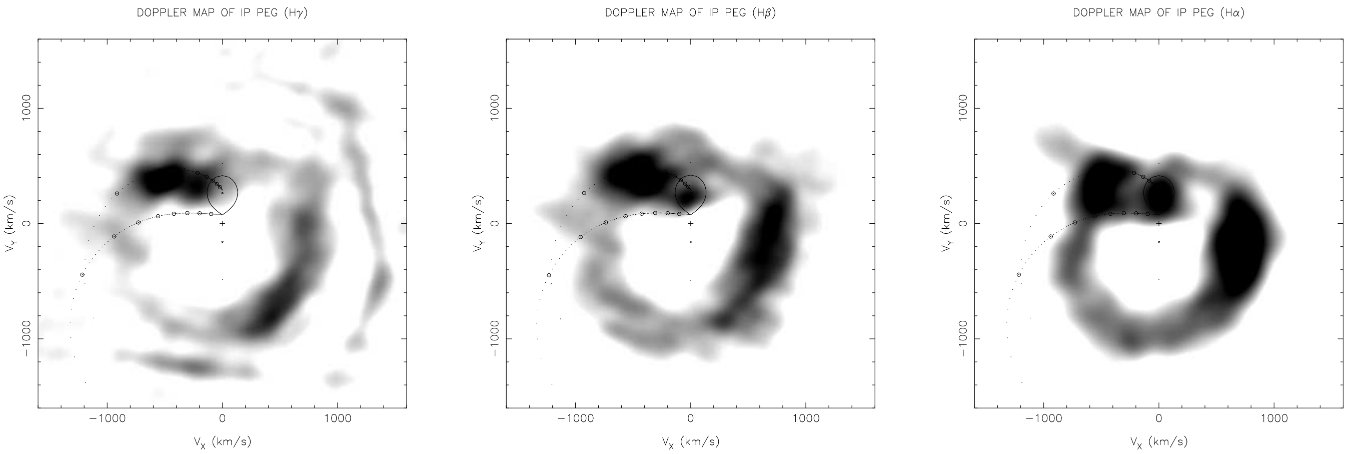

Fig. 7. Doppler maps of the prominent Balmer lines Hγ, Hβ and Hα in velocity space (V_X, V_Y) using the Fourier–filtered back–projection technique. The intense small spot around V_Y = 300 kms^{-1} in the Hβ and Hα map represents the heated surface of the secondary, whereas the smaller bright emitting region extending with velocity coordinates $V_X \approx -200\ldots-800$ kms^{-1}, $V_Y \approx 200\ldots600$ kms^{-1} can be contributed to emission coming from the hot spot on the outer regions of the accretion disk. The origin of the larger bright emitting region with velocity coordinates of $V_X \approx 200\ldots800$ kms^{-1}, $V_Y \approx -900\ldots300$ kms^{-1} is not ascertained. It can be either explained as the beginning of the formation of a spiral arm or a second inner spot due to returning material from a ricocheted gas stream. Sampling errors are represented by aliasing streaks in the higher velocity regions. A schematic overlay marks the Roche–lobe of the secondary as well as the ballistic trajectory which originates from the L_1 point. Additionally plotted is a second trajectory which represents the velocity of the disk along the path of the gas stream. Further information for each line is given in the text.

Sect. 2.1) in order to remove the atmospheric effects from the non–photometric parts of the relevant eclipse–observations. The Balmer lines and the underlying continuum, were extracted as described in Sect. 2.2. In order to improve the signal to noise ratio we also phase–folded the data of the second and third night. The first night was omitted because the eclipse was not totally recorded (see Fig. 3).

4.2.2. The Continuum

First we will examine the continuum data and discuss the main properties by taking the Hβ emission line as an example. The light curve and its reconstructions are plotted in Fig. 8 and show a clear and strong hump structure and a weak disk/dwarf component.

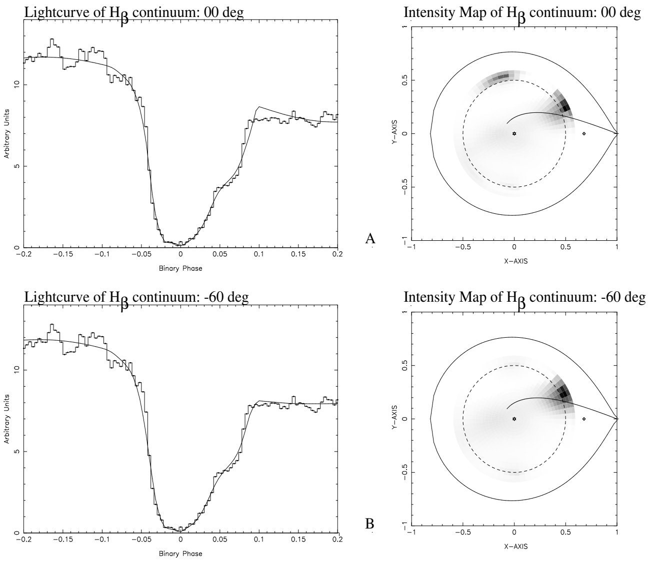

Fig. 8. A: Reconstruction of the Hβ continuum light curve using the eclipse mapping algorithm. The left panel shows the data with the fit (solid line). The right panel shows the reconstructed intensity map of Hβ. The dashed circle represents the outer disk radius. Pixels outside the dashed circle belong to the rim and are folded upward for plotting reasons. The tilt angle of the pixels in in the hot spot region is $-0°$.
B: The same as A but the pixels in in the hot spot region are this time tilted outward by $-60°$.

Our eclipse mapping algorithm was not able to reconstruct the egress feature of the hot spot located roughly at phase 0.09 (see Fig. 8A left panel). Figure 8A (right panel) shows the reconstructed map in the orbital plane. A schematic overlay on the eclipse maps of the disk marks the primary's Roche lobe and the gas stream trajectory. The white dwarf is centered at the (0;0) position in the coordinate system. The unit of this system is the distance from the white dwarf to the inner Lagrangian point. The center of mass is also marked in the plots. The position of the secondary at the outer right–hand side of the frame is not shown in the following figures. The dashed circle represents

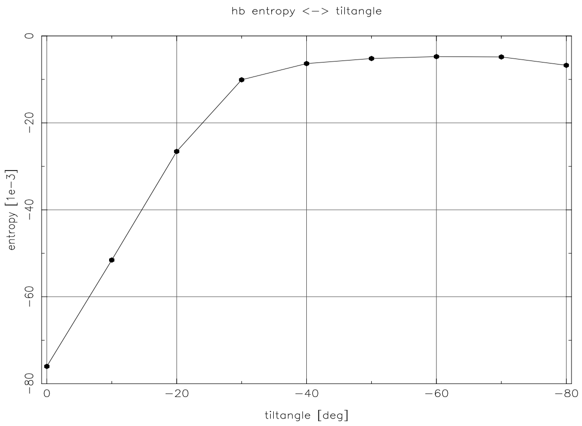

Fig. 9. The entropy for Hβ eclipse mapping reconstruction is plotted versus the tilt angle in the hot spot region. Negative angles stand for tilting the pixels outward (i.e. away from the secondary). The angles are measured between the tilted and untilted direction of a vector standing perpendicularly on the surface element.

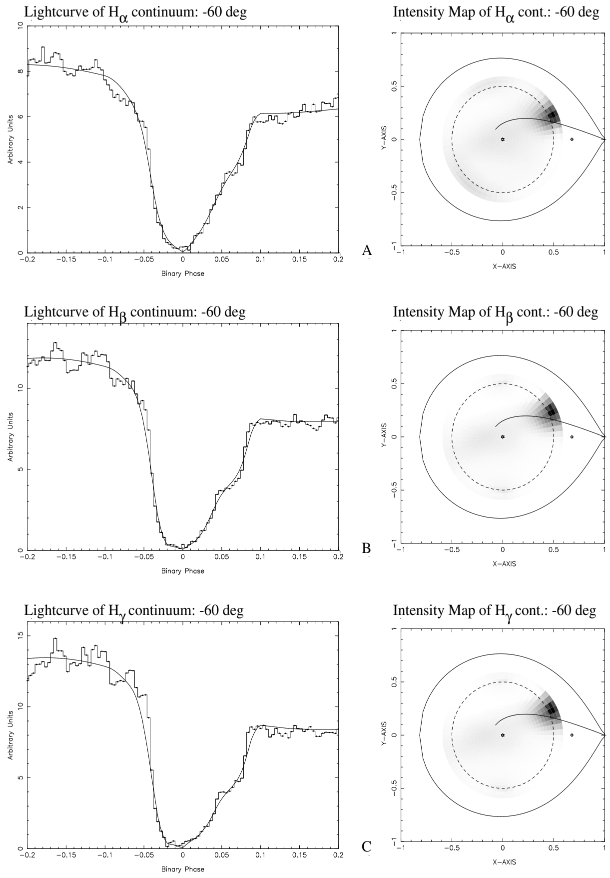

Fig. 10. A: Reconstruction of the Hα continuum light curve using the eclipse mapping algorithm. The left panel shows the data with the fit (solid line). The right panel shows the reconstructed intensity map in Hα. The dashed circle represents the disks outer radius. Pixels outside the dashed circle belong to the rim and are folded upward for plotting reasons. The pixels in in the hot spot region are tilted outward by $-60°$.
B: Like A but for Hβ; C: Like A but for Hγ

the outer edge of the disk. The pixels outside the dashed circle depict the (for plotting reasons) upward folded rim within the range of three pixel rows.

The reconstruction (Fig. 8A right) shows a clear feature of the hot spot (at the position (0,5;0.2)) directly on the rim. In the center of the disk a faint continuum emission can be seen, but the emission from the white dwarf is completely smeared out and vanishes under the central disk emission. This might have two reasons. First, the only information in the light curve about the primary star is its egress feature at phase 0.04 (see Fig. 8A left). The ingress is completely blended with the ingress of the hot spot. Second, the feature of the primary's egress is of the same order as the flickering and therefore negligible. Thus, the hot spot is the main contributor to the continuum emission in the disk. Nevertheless, a second spot appears at the upper rim (at (-0.1;0.5) in Fig. 8A right). This structure is a so–called 'reconstruction ghost' and arises from the fact that the reconstruction algorithm assumes that all rim pixels are radiating radially outward. The hot spot seems to have a more complicate radiation behaviour. Its main radiation direction seems to be tilted outward (i.e. away from the gasstream).

To test this idea we created artificial disks with tilted impact regions, made light curves with artificial noise and reconstructed the disk. In these simulations the ghost hot spot also appeared. The structure vanished when the right tilt angle was introduced for the reconstruction-map. It was possible to detect the correct tilt angle with an accuracy of $\pm 10°$ or $\pm 20°$ for a signal to noise ratio of 50 or 10, respectively.

After that, the map-pixels in the stream impact region were tilted outward. The tilt angle was measured with respect to the line between the white dwarf and the crossing point of the gas stream with the outer disk radius. We give the tilt angle a negative value for outward tilting and a positive value for inward tilting (i.e. towards the secondary). The quality of a reconstruction can be seen directly via the entropy. We tilted the impact region pixels in $-10°$ steps outward (inward tilting did not provide good results) and plotted the final entropy versus the tilt angle in Fig. 9.

Our final entropy shows a broad and flat maximum at $-60°$ and a steep rising from 0° to $-30°$ from where on the broad maximum begins. How the reconstruction of Hβ for a tilt angle of $-60°$ is influenced is shown in Fig. 8B. It can be clearly seen that the ghost hot spot has vanished and the egress feature of the hot spot at phase 0.09 in the light curve is reconstructed very well.

This behaviour is very similar for the Hα and Hγ continuum, too. It seems that red lines have larger tilt angles and blue lines smaller, but all lie between $-50°$ and $-80°$. The reconstructions are all very similar between $-50°$ and $-80°$ and for all cases no significant difference can be recognized.

We therefore present our results for Hα, Hβ and Hγ continuum reconstruction for tilt angles with $-60°$. The light curves and the maps are shown in Fig. 10.

4.2.3. The Lines

The reconstructions of the Balmer emission line maps were done in the same manner as the continuum line maps, using the same tilt angle of $-60°$. But in contrary to the continuum maps (R_{disk} =0.5 R_{L1}) a slightly increased disk radius of R_{disk} =0.55 R_{L1} was chosen. The disk radius used for the reconstructions was determined from the geometric system parameters and the duration of the disk eclipse. For details see Sulkanen et al. (1981).

In Fig. 7 we have seen that the intensity of the disk in velocity space shows a particular asymmetric intensity distribution. The hot spot is clearly present at its common location, but at higher V_x velocities the disk is brightened. This location relates in the space–coordinate representation to this region where the disk's material has circled the center by more than one half and is moving into the direction towards the secondary star (see also Fig. 7). In the eclipse-maps this region corresponds to the lower half of the disk. If the brightened region in the Doppler maps corresponds to a real region in the disk, and is not some strange velocity artifact or a 'shining through' of the main hot spot, it should be recoverable in the eclipse maps. The dataset from which the Doppler maps were calculated, has high spectral resolution, but a low time resolution. MEKASPEK provides high time resolved data with low spectral resolution. A higher spectral resolution is also present in the MEKASPEK data, but it is very well hidden in the shape of the high–speed data of the

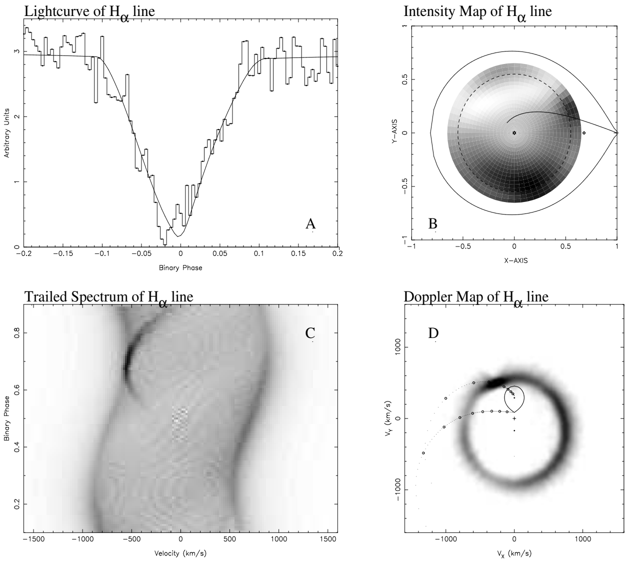

Fig. 11. A: Fit to the data of the Hα emission light curve. The solid line is the maximum entropy fit. B: Reconstructed intensity map for Hα. The dashed circle represents the outer disk radius. Pixels outside the dashed circle belong to the rim and are folded upward for plotting reasons. The tilt angle of the pixels in the hot spot region is $-60°$. C: Spectrum calculated via a Keplerian velocity field from the Hα map plotted in B with a tiltangle of $-60°$. D: Doppler map for Hα, computed from the trailed spectrum displayed in C.

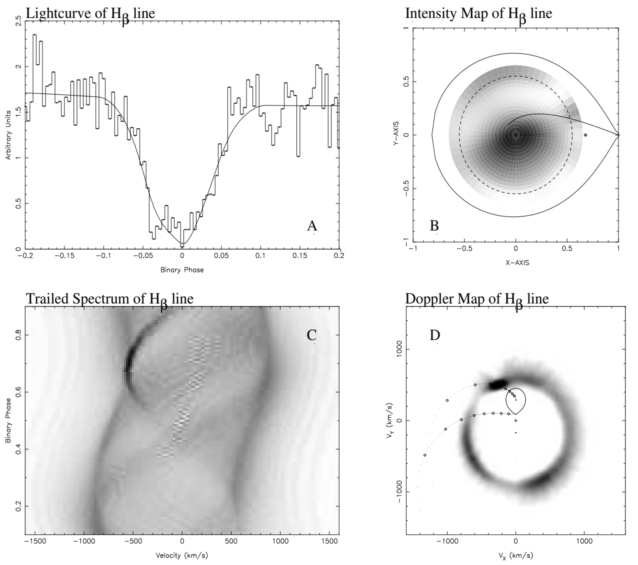

Fig. 12. A: Fit to the data of the Hβ emission light curve. The solid line is the maximum entropy fit. B: Reconstructed intensity map for Hβ. The dashed circle represents the outer disk radius. Pixels outside the dashed circle belong to the rim and are folded upward for plotting reasons. The tilt angle of the pixels in the hot spot region is $-60°$. C: Spectrum calculated via a Keplerian velocity field from the Hβ map plotted in B with tiltangle $-60°$. D: Doppler map for Hβ, computed from the trailed spectrum displayed in C.

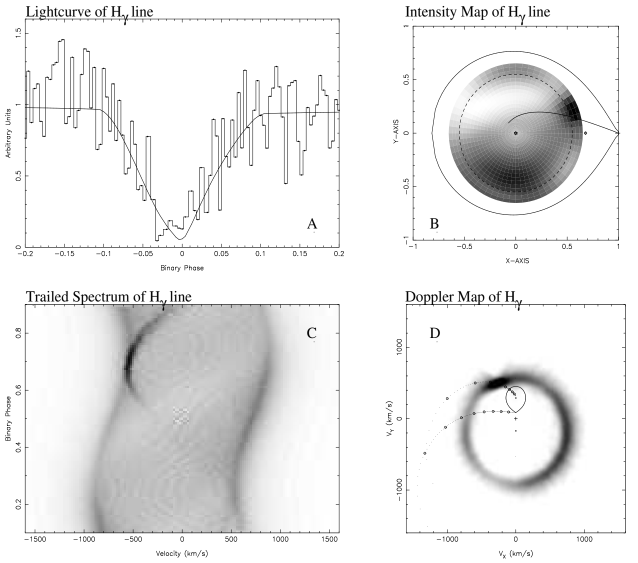

Fig. 13. A: Fit to the data of the Hγ emission light curve. The solid line is the maximum entropy fit. B: Reconstructed intensity map for Hγ. The dashed circle represents the outer disk radius. Pixels outside the dashed circle belong to the rim and are folded upward for plotting reasons. The tilt angle of the pixels in the hot spot region is $-60°$. C: Spectrum calculated via a Keplerian velocity field from the Hγ map plotted in B with tiltangle $-60°$. D: Doppler map for Hγ, computed from the trailed spectrum displayed in C.

eclipse. The eclipse tells us the distribution of intensity in the space–coordinate representation of the disk.

The (high resolution) spectra we detect are nothing more than the transformed information of the intensity via an unknown velocity field. Converting the reconstructed intensity distribution in space–coordinate representation via an assumed velocity field into spectra unpacks the spectral resolution which was hidden in the eclipse.

Disks are assumed to rotate in a Keplerian velocity field, with the exception of the hot spot region, were the velocities from the disks outer rim and the impacting gas stream are mixed.

Doppler tomography makes no assumption about any velocity field, but one has to make one to convert the maps derived via eclipse mapping into spectra. We note, that a Keplerian behavior of the whole disk was assumed in order to transform the reconstructed maps into spectra. These spectra, derived from the eclipse mapping method were used again in order to compute Doppler maps in velocity space. Figures 11, 12 and 13 show our results for the three Balmer lines Hα, Hβ and Hγ. The panels denoted by A show the emission line light curve and the fit (solid line). Panels B present the reconstructed maps received via eclipse mapping. In panels C the spectra calculated from the maps shown in B via Kepler velocity field are plotted. These spectra were the input for the Doppler tomography. The reconstructed Doppler maps are shown in panels denoted by D.

In the continuum maps only the hot spot is dominant because of its high temperature. The eclipse mapping emission line maps show both emission from the hot spot and emission from the disk. The emission line light curves show only a very faint hump, so the disk is the main contributor for the emission line–flux. But nevertheless, the emission line maps show also an asymmetric light–flux distribution. They are brighter in a region "below" the white dwarf, corresponding to high positive V_x and low $\pm V_y$ velocities (see Fig. 5 phase point 7).

The Hα and Hγ eclipse maps (panels B) are very similar. The Hβ map deviates from the others, since the Hβ line was at the edge of the MEKASPEK detector for the blue part of the spectrum and might be somewhat distorted. Therefore this map is less reliable than the others.

The Doppler maps made out of the spectra from the eclipse maps are very similar to the original Doppler maps derived from the high resolution spectra. They also show a brightened region at high positive V_x velocities. However they are smeared out because of the application of a maximum entropy algorithm to derive the eclipse maps. So the 'spots' are not so prominent as in the original Doppler maps but still visible.

A slight difference is that the main hot spot is shifted compared with the original Doppler maps and hits exactly the Kepler–trajectory. In the original Doppler maps the hot spot is roughly between or under the Kepler–trajectory of the gas stream (see Fig. 7). This can be easily explained with our assumption of a Keplerian disk when converting the eclipse maps into spectra. However, the hot spot region is not Keplerian.

5. Discussion

After the analysis of our datasets we present in this section a discussion of the probable origin of the detected multi–emission sites in the accretion disk of IP Peg.

By combining Doppler tomography which reconstructs maps from emission line spectra (using only out–of eclipse data, since there is no relation between position and velocity during eclipse) and the eclipse mapping method which reconstructs intensity maps from emission line light curves (using information of ingress and egress features of the disk components during eclipse) we were able to detect independently corresponding multi emission sites in the accretion disk in velocity as well as in spatial coordinates.

Two models are currently being discussed to explain the above described emission regions. As already mentioned in Sect. 4.1. Armitage & Livio (1996) presented Smooth Particle Hydrodynamics (SPH) simulations of a stream overflow which results from the collision of the accretion stream with the disk rim. From there on, this material is swung over the disk plane where it is accelerated by the strong gravity of the white dwarf. It hits the inner disk regions, creating a second bright spot on a roughly diametrically opposed side of the first hot spot.

Our Doppler and eclipse maps might confirm these calculations, since we can clearly locate two bright emitting regions in velocity as well as spatial coordinates which are opposed almost diametrically to each other. We would like to note though, that these SPH simulations were performed only for low mass X–ray binaries, whose accretion and outburst behaviour cannot be entirely compared with IP Peg.

The second model which has to be considered, are spiral structures in the accretion disk, as first detected by Steeghs et al. (1997). Their Doppler maps of IP Peg in outburst show first observational evidence of a two–armed spiral pattern. The origin of this pattern might be due to a tidal interaction of a large disk with the companion star. As explained and predicted in theory, the tides induced by the secondary can excite waves in the outer disk.

Our structures in the Doppler as well as in the eclipse maps cannot give an unequivocal confirmation of a spiral pattern. As already noticed in Sect. 4.1., our observed structures might be explained with the beginning of the generation of a spiral wave, since the accretion disk seems to be more extended and therefore larger than in other observed quiescence states. And in fact, IP Peg was observed in an unusual strong outburst almost three weeks after our observation run (Nogami 1995).

Another criterion in favour of this model is an analytical work by Bunk et al. (1990). The author's calculations indicated that a spiral shock leads to a change in the width of the eclipse light curve and therefore to an asymmetry. The best signature of the presence of shocks should be observable in ultraviolet eclipse light curves. They also noted that the effect of shocks on the optical light curves is small ($\Delta m \approx 0.07$) but is still well within the differential accuracy of modern photometry.

We observed a rather small but distinguishable asymmetry in our emission line light curves, an effect also stated by Marsh (1988). The author explained that this asymmetric, more extended ingress duration (see also Fig. 4) is indicative of a distortion of the disk due to the interaction of the stream with the disk rim.

The asymmetry in the emission line light curves varies from quiescent to outburst states and the explanations of this feature can sometimes be puzzling. Nogami's (1995) eclipse light-curves show an asymmetry of the eclipse profile developing with time, during rising, maximum outburst and declining phase of IP Peg. The author refrained from a further interpretation.

Although our interpretations and comparisons with already published works seem to favour the spiral structure model, definitive answers for the nature and origin of the multi–emission sites in the accretion disk of IP Peg can only be given by simultaneous spectroscopic and spectrophotometric measurements at large telescopes. These observations would significantly improve the spatial resolution of the eclipse maps and therefore resolve the signatures of these interesting regions.

6. Summary

We have presented high–resolution spectroscopy and high–speed–spectrophotometry of the eclipsing dwarf nova IP Peg during quiescence. By combining the two observational methods we were able to calibrate the continuum of the spectroscopic data set with the atmospheric–extinction–free continuum of the reduced spectrophotometric data set. Thus, it was possible to investigate separately emission line and continuum light curves. The analysis and interpretation of our data set revealed that this system was on the rise to an outburst. The typical Doppler broadened Balmer emission lines Hδ, Hγ, Hβ, Hα were accompanied with the TiO absorption bands as well as the KI and NaI absorption doublets. A weak *s-wave* moving with the radial velocity amplitude of the secondary could be observed in the phase range $\varphi \approx 0.4 \ldots 0.6$ of the Balmer lines Hβ and Hα. This behaviour is indicative for an enlarged accretion disk prior to an outburst, and indeed IP Peg was in maximum outburst almost three weeks later (Nogami 1995).

With the means of Doppler tomography we could clearly locate the above mentioned *s-wave* on the irradiated face of the secondary star. Next to the typical ring–like distribution characteristic for a Doppler map of a quiescent accretion disk we could also find two peculiar bright spots superposed to the emission ring. The smaller one can be contributed to emission coming from the hot spot. The larger one can be interpreted with the beginning of the formation of a spiral arm which might be due to tidal interference of the secondary star onto the extended accretion disk, as first observed and explained by Steeghs et al. (1997) and Harlaftis & Steeghs (1997). Another explanation of this large emitting region could be a second, inner hot spot due to a gas stream overflow, an effect suggested by simulations of Armitage & Livio (1996).

By analysing the decomposed light curves of our simultaneously recorded spectrophotometric data set we found in the continuum light curves a second hump around phase $\varphi \approx 0.3 \ldots 0.4$ separated by ≈ 0.5 phase units from the well known strong orbital hump. The intensity of the second hump is essentially weaker by a factor of 2.

The emission line light curves reveal a slight asymmetric V–like eclipse of the accretion disk by the secondary star. Almost no hump signatures could be detected.

We have shown that it is possible to make eclipse maps out of emission line light curves and that the reconstructed trailed spectra and Doppler maps are in good agreement with the high resolution Doppler maps, with the exception of the hot spot region. Our conclusion from the eclipse mapping method combined with Doppler tomography, is that the disk is mainly a Keplerian disk and that the deviation from the Keplerian field in the hot spot region can be roughly measured by comparing these maps with the original high resolution Doppler maps. It was also shown, that the bright region appearing in our high resolution Doppler maps is associated with a geometrically detectable region via eclipse mapping.

The eclipse mapping method gives information about the location of a certain intensity, the Doppler tomography about its velocity. By comparing the results of both methods, velocity fields in other CVs could be measured and thus provide more information about the origin of multi–emission sites. Further analysis on larger telescopes is strongly encouraged since the possible explanations for the origin an nature of these features are correlated with the two competing models for outburst, the disk instability (i.e. Meyer & Meyer–Hofmeister 1981) or the mass transfer outburst model (Bath & Pringle 1981).

Acknowledgments

The authors are grateful to Niv Drory, Alex Fiedler, Hauke Fiedler, Viki Joergens and Sonja Wolf for assistance and many fruitful discussions. We are especially thankful to Hans-Christoph Thomas for his remarks on our manuscript, to Hans Ritter for drawing our attention to the work of Bunk et al. (1990) and to the anonymous referee for his useful comments. In particular we would like to thank Rick Hessman for advice during the observation run.

References

Armitage P.J., Livio M., 1996, ApJ, 470, 1024
Baptista R., Steiner J.E., 1993, A&A, 277, 331
Barwig H., Schoembs H., Buckenmayer C., 1987, A&A, 175, 327
Bath G.T., Pringle J.E., 1981, MNRAS, 194, 976
Bunk W., Livio M., Verbunt F., 1990, A&A, 232, 371
Bevington P.R., Robinson D., 1992, Data reduction and error analysis for the physical sciences, McGraw–Hill Inc., New York
Bobinger A., Horne K., Mantel K.H., Wolf S., 1997, A&A, 327, 1023
Diaz M.P., Steiner J.E., 1994, A&A, 283, 508
Goranskij V.P., Shugarov S.Yu., Orlowsky E.I., Rachimow V.Yu., 1985, Inf. Bull. of Var. Stars, 2653
Harlaftis E.T., Steeghs D., 1997, Spectrum PPARC, 13, 4
Harlaftis E.T., Marsh T.R., Dhillon V.S., Charles P.A., 1994, MNRAS, 267, 473
Hessman F.V., 1989, AJ, 98, 675
Horne K., 1985, MNRAS, 213, 129
Horne K., 1986, PASP, 98, 609
Horne K., 1991, In: Fundamental Properties of Cataclysmic Variable Stars: 12th North American Workshop on Cataclysmic Variables and Low Mass X–ray Binaries, San Diego, San Diego State University Publication, p. 23
Horne K., 1995, A&A, 297, 273.
Horne K., Cook M.C., 1985, MNRAS, 216, 307
Horne K., Marsh T.R., 1986, MNRAS, 218, 761
Horne K., Stiening R.F., 1985, MNRAS, 216, 933
Horne K., Marsh T.R., Cheng F.H., Hubeny I., Lanz T., 1994, ApJ, 426, 294
Kaitchuck R.H., Schlegel E.M., Honeycutt R.K., et al. , 1994, ApJ, 93, 519
Lipovetskij V.A., Stephanyan J.A., 1981, Afz, 17, 573
Mantel K.H., Barwig H., 1993, NATO ASI series, C436, 329
Mantel K.H., Barwig H., Kiesewetter S., 1993b, AG Abstract series, 9, 14
Marsh T.R., 1988, MNRAS, 231, 1117
Marsh T.R., Horne K., 1988, MNRAS, 235, 269
Marsh T.R., Horne K., 1990, ApJ, 349, 593
Martin J.S., Friend M.T., Smith R.C., Jones D.H.P., 1989, MNRAS, 240, 519
Meyer F., Meyer–Hofmeister E., 1981, A&A, 104, L10
Nogami D., 1995, In: Basic Physics of Accretion Disks, eds.: Kato, S. et al. , Gordon and Breach Science Publishers
Robinson E.L., Marsh T.R., Smak J.I., 1993, In: Accretion Disks in Compact Stellar Systems, Singapore, World Scientific Publishing Co. Pte. Ltd, p.75
Rutten R.G.M., van Paradijs J., Tinbergen J., 1992a, A&A, 260, 213
Rutten R.G.M., Kuulkers E., Vogt N., van Paradijs J., 1992b, A&A, 265, 195
Shafter A.W., 1985, in: Cataclysmic Variables and Low–Mass X–Ray Binaries, ed.D.Q. Lamb & J. Patterson (Dordrecht: Reidel), p.355
Šimić D., Barwig H., Bobinger A., Mantel K.H., Wolf S., 1998, A&A, 329, 115
Skilling J., Bryan R.K., 1984, MNRAS, 211, 111
Steeghs D., Horne K., Marsh T.R., Donati J.F., 1996, MNRAS, 281, 626
Steeghs D., Harlaftis E.T., Marsh T.R., Horne K., 1997, MNRAS, 290, L28
Sulkanen M.E., Brasure L.W., Patterson J., 1981, ApJ, 224, 579
Szkody P., Mateo M., 1986, AJ, 92, 483
Wolf S., Mantel K.H., Horne K., et al. , 1993, A&A, 273, 160
Wood J.H., Crawford C.S., 1986, MNRAS, 222, 645
Wood J.H., Marsh T.R., Robinson E.L., Stiening R.F., Horne K., 1989, MNRAS, 239, 809
Wood J.H., Abbot T.M.C., Shafter A.W., 1992, ApJ, 393, 729

A. The determination of radial velocities

A.1. The radial velocity of the secondary star

The usual approach in obtaining the radial velocity of the secondary star is measuring the radial velocity semi–amplitude of the absorption lines. Our investigation was restricted to the strong absorption line doublets KI and NaI. We fitted a single Gaussian to every absorption line profile. In order to suppress the influence of noise in these spectra and to provide a reliable profile fit, the central region of the Gaussians was given a bigger weight with respect to the adjacence (continuum–transition) of the line profiles. After that, a sine–fit was applied to the fitted radial velocity V of the observed semi–amplitudes $K_{obs.}$ using the following relation :

$$V = \gamma + K_{obs.} \sin(\varphi - \varphi_0) \quad \text{(A1)}$$

where γ is the system velocity, and $K_{obs.}$ denotes the observed radial velocity semi–amplitude of the secondary star. φ and φ_0 respectively indicate the phase and the phase offset of the binary system. The sine–fit to the radial velocity curve of the secondary star are presented in Fig. 3, whereas the deduced orbital parameters are displayed in Table. 3. After computing a mean system velocity from the four measured absorption lines we kept γ and φ_0 fixed, since one can generally assume that the orbits of CVs are circularized by tidal dissipation. This was also done in order to adapt the determination of the radial velocity and the corresponding error.

Table 3. Orbital parameter for IP Peg. $K_{obs.}$ is the observed semi–amplitude of the radial velocity of the secondary star and γ denotes the system velocity, both in kms^{-1}, φ_0 designates the phase–offset of this system. σ designates the errors of the mentioned parameter. $KI_{a,b}$ represents the KI absorption doublet ($\lambda\lambda$ 7665, 7699), whereas $NaI_{a,b}$ represents the NaI absorption doublet ($\lambda\lambda$ 8183, 8195). $\overline{K_{obs.}}$, $\overline{\gamma}$, and $\overline{\varphi_0}$ are the deduced mean values of the mentioned parameter, whereas $\overline{\sigma}$ is their corresponding mean error.

Line	$K_{obs.}$	$\sigma K_{obs.}$	γ	σ_γ	φ_0	σ_φ	Data
KI_a	275.05	2.33	29.00	3.46	0.5	0.0	432
KI_b	276.79	2.59	29.00	3.46	0.5	0.0	356
NaI_a	266.08	1.95	29.00	3.46	0.5	0.0	478
NaI_b	274.01	1.88	29.00	3.46	0.5	0.0	389
Line	$\overline{K_{obs.}}$	$\overline{\sigma K_{obs.}}$	$\overline{\gamma}$	$\overline{\sigma_\gamma}$	$\overline{\varphi_0}$	$\overline{\sigma_\varphi}$	Data
Mean	272.03	2.09	29.00	3.46	0.5	0.0	1656

According to Martin et al. (1989) the geometric distortion of the secondary star shifts its photometric centre towards the centre of the system, resulting in a K_{abs}–semi–amplitude of the absorption lines slightly smaller ($\approx$ 3%) than the true semi–amplitude of the centre of mass motion (K_2).

A proper correction for $K_{obs.}$ could in principle be derived by adjusting the absorption line strength to match the phase-dependent line–flux. However, due to poor S/N of our line flux light curves, we were not able to apply this more accurate correction.

Therefore, we only corrected our slightly smaller K_{Na} semi–amplitude as suggested by Martin et al. (1989) and obtained a new value for the semi–amplitude of the secondary star of IP Peg K_2=280 $\pm$ 2 kms^{-1}.

It should be stressed that the errors in Tab. 3 are estimated errors, assuming equal weighting for each Gaussian fitted radial velocity. Determination of errors was done according to the procedure described in Bevington & Robinson (1992).

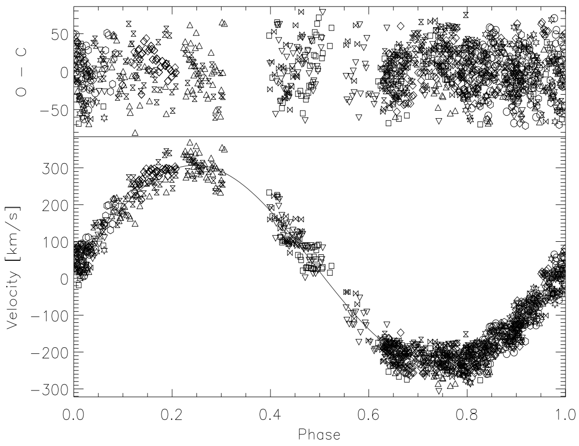

Fig. 14. Radial velocity curve for the secondary star determined by fitting Gaussians to the KI and NaI absorption line doublets. The upper panel shows the residuals, the lower the distribution of the fitted data. The phase–range runs along the abscissa and the velocity along the ordinate. Different symbols mark the three consecutive observing nights. The deduced radial velocities for each absorption line are shown in Table 3.

A.2. The radial velocity of the primary star

Emission lines of CVs have confronted observers with many difficulties. A major problem has been the inability to reliably determine the radial velocity of the primary star, which is needed in order to derive its mass. Unfortunately, in many CVs the white dwarf is not detected directly, and therefore disk emission lines are measured. The most common technique is to exclude the emission line cores and use only the emission line wings for radial velocity determination. They are generally assumed to be undisturbed by the *s-wave*, while the light in these wings, coming from the inner disk, can provide information about the primary's orbital motion (e.g. Shafter (1985)).

Our attempts to derive reliable radial velocities from the measurement of the line wings failed, since the continuum light contribution of the white dwarf in quiescence is only about 10% (Marsh 1988).

Therefore, the effect of the white dwarf in the photospheric absorption lines in the emission line wings is minor and the general poor S/N of trailed spectra additionally distort the wing profiles. We obtained the primary's radial velocity indirectly by using the photometrically calculated mass ratio from Wolf et al. (1993) with the following relation :

$$K_1 = qK_2 \quad \text{(A2)}$$

where q = 0.6 $\pm$ 0.1 is the mass ratio, and K_2=280 $\pm$ 2 kms^{-1} denotes the radial velocity semi–amplitude of the secondary star, determined in the above section. The indirectly obtained velocity of the semi–amplitude of the white dwarf therefore amounts to K_1 = 168 $\pm$ 30 kms^{-1}.

This article was processed by the author using Springer-Verlag LaTeX A&A style file *L-AA* version 3.